

Measurements of Charged Current Reactions of ν_e on ^{12}C

L.B. Auerbach,⁸ R.L. Burman,⁵ D.O. Caldwell,³ E.D. Church,¹
 J.B. Donahue,⁵ A. Fazely,⁷ G.T. Garvey,⁵ R.M. Gunasingha,⁷ R. Imlay,⁶
 W.C. Louis,⁵ R. Majkic,⁸ A. Malik,⁶ W. Metcalf,⁶ G.B. Mills,⁵
 V. Sandberg,⁵ D. Smith,⁴ I. Stancu,¹*M. Sung,⁶ R. Tayloe,^{5†}
 G.J. VanDalen,¹ W. Vernon,² N. Wadia,⁶ D.H. White,⁵ S. Yellin³
 (LSND Collaboration)

¹ University of California, Riverside, CA 92521

² University of California, San Diego, CA 92093

³ University of California, Santa Barbara, CA 93106

⁴ Embry Riddle Aeronautical University, Prescott, AZ 86301

⁵ Los Alamos National Laboratory, Los Alamos, NM 87545

⁶ Louisiana State University, Baton Rouge, LA 70803

⁷ Southern University, Baton Rouge, LA 70813

⁸ Temple University, Philadelphia, PA 19122

February 26, 2019

Abstract

Charged Current reactions of ν_e on ^{12}C have been studied using a μ^+ decay-at-rest ν_e beam at the Los Alamos Neutron Science Center. The cross section for the exclusive reaction $^{12}C(\nu_e, e^-)^{12}N_{g.s.}$ was measured to be $(8.9 \pm 0.3 \pm 0.9) \times 10^{-42}$ cm². The observed energy dependence of the cross section and angular distribution of the outgoing electron agree well with theoretical expectations. Measurements are also presented for inclusive transitions to ^{12}N excited states, $^{12}C(\nu_e, e^-)^{12}N^*$ and compared with theoretical expectations. The measured cross section, $(4.5 \pm 0.4 \pm 0.6) \times 10^{-42}$ cm², is somewhat lower than previous measurements and than a continuum random phase approximation calculation. It is in better agreement with a recent shell model calculation.

*now at University of Alabama, Tuscaloosa, AL 35487

†now at Indiana University, Bloomington, IN 47405

1 Introduction

In recent years neutrino interactions with nuclear targets have been used to detect low energy neutrinos (< 500 MeV) from many sources: solar, atmospheric, supernova explosions, reactors and accelerators. An understanding of the nuclear cross sections is necessary for interpretation of the measurements. Especially important nuclei are ^{12}C and ^{16}O because of the widespread use of oil and water detectors.

Many calculation techniques have been used to determine neutrino-nuclear cross sections. Shell model techniques work best at lower energies where transitions to continuum states are not large. At intermediate energies the Continuum Random Phase Approximation (CRPA) is frequently used, while at still higher energies the Fermi gas model is thought to work well. Comparison of different calculations of the cross section for a particular process can provide an indication of the uncertainty involved. Experimental measurements of some cross sections are, however, necessary to establish the range of validity of the different calculation techniques.

Relatively few measurements of neutrino-nucleus cross sections exist in the energy region of the present experiment, $E_\nu < 52.8$ MeV. The best measured nucleus is carbon for which three experiments, including the Liquid Scintillator Neutrino Detector (LSND) experiment, have previously reported results. E225[1] at LAMPF, the KARMEN Collaboration[2] at the ISIS facility of the Rutherford Laboratory and LSND[3] have measured the cross section for the exclusive reaction $^{12}C(\nu_e, e^-)^{12}N_{g.s.}$ and for the inclusive reaction $^{12}C(\nu_e, e^-)^{12}N^*$ to all other accessible ^{12}N final states. The ^{12}N ground state reaction dominates the total yield as it is the only allowed ($l = 0$) transition that occurs in this process. The cross section for producing the ^{12}N ground state can be calculated to an accuracy of 2% as it can be represented in terms of form factors[4] that can be reliably extracted from other measurements. Calculation of the inclusive cross section for transitions to excited states of ^{12}N is much less straightforward. Various theoretical techniques, each with their own strengths and limitations, have been used to calculate the cross section[5, 6, 7, 8, 9, 10, 11]. Comparison with measurements may help clarify the theoretical picture. In this paper we report our final results for these processes, including measurements of the angular distribution of the electron with respect to the ν_e direction and the energy dependence of the ground state transition.

Measurements also exist for two processes closely related to ν_e carbon scattering: μ^- capture on ^{12}C [12] and ν_μ scattering on carbon using a beam of ν_μ from π^+ decay-in-flight (DIF)[13]. For the ν_e carbon measurement $E_\nu \approx 32$ MeV, $Q \approx 50$ MeV/c and the inclusive cross section is dominated by transitions to low multipoles ($1^+, 1^-, 2^-$). In contrast, for the ν_μ carbon measurement $E_\nu \approx 180$ MeV, $Q \approx 200$ MeV/c and excitations occur up to 100 MeV. The μ^- capture process, which occurs from the S state, is intermediate between these two processes with $Q \approx 90$ MeV/c. Because these three processes occur

at different energies and momentum transfers they constrain different aspects of theoretical calculations. A good test of a theoretical procedure is its ability to predict all three processes.

The measurement[13] of the inclusive cross section for $^{12}C(\nu_\mu, \mu^-)^{12}N^*$ several years ago by LSND attracted substantial interest because a CRPA calculation[6] predicted a cross section almost twice as large as that observed. An improved calculation by the same group[7] together with an improved calculation of the neutrino energy spectrum and flux has reduced but not eliminated the discrepancy with the measured cross section. Recent calculations using the shell model[8, 9] are in better agreement with the measured cross section.

Hayes and Towner[9] calculated a cross section of $4.1 \times 10^{-42} \text{ cm}^2$ for the process $^{12}C(\nu_e, e^-)^{12}N^*$ using the same shell model procedure that provided the best agreement with data for the reaction $^{12}C(\nu_\mu, \mu^-)^{12}N^*$. This is lower than both the earlier[6] and the more recent[7] CRPA calculations by Kolbe *et al.* of $6.3 \times 10^{-42} \text{ cm}^2$ and $5.5 \times 10^{-42} \text{ cm}^2$ respectively. Thus measurements of this cross section can provide a useful test of the relative merits of the different theoretical techniques that have been used.

2 The Neutrino Source

The data reported here were obtained between 1994 and 1997 at the Los Alamos Neutron Science Center (LANSCE) using neutrinos produced at the A6 proton beam stop. We chose to exclude data obtained in 1998 from this analysis because only electrons with reconstructed energies above 20.4 MeV were fully processed for that year's data. Since this analysis is dominated by systematics we decided to limit our analysis to the 1994-1997 data which has a uniform efficiency above 18 MeV. The neutrino source is described in detail elsewhere[14]. In 1994 and 1995 the beam stop consisted of a 30 cm water target surrounded by steel shielding and followed by a copper beam dump. The high-intensity 798 MeV proton beam from the linear accelerator generated a large pion flux from the water target. The flux of ν_e used for the measurements reported here arise from the decay at rest (DAR) of stopped π^+ and μ^+ . This decay chain yields almost equal intensities of ν_e , $\bar{\nu}_\mu$ and ν_μ with the well-determined energy spectra shown in Fig. 1.

After the 1995 run the beam stop was substantially modified for accelerator production of tritium (APT) tests. The most significant change for the analysis presented in this paper was the replacement of the water target by tungsten and other materials with high atomic number. This resulted in reduced π^+ production and a lower DAR neutrino flux, largely due to the change in the neutron to proton ratio in the target.

The corresponding decay chain for π^- and μ^- is highly suppressed due to three factors. First, production of π^- is smaller than for π^+ . Second, π^- which stop are absorbed by nuclear interactions. Finally, most μ^- which stop are

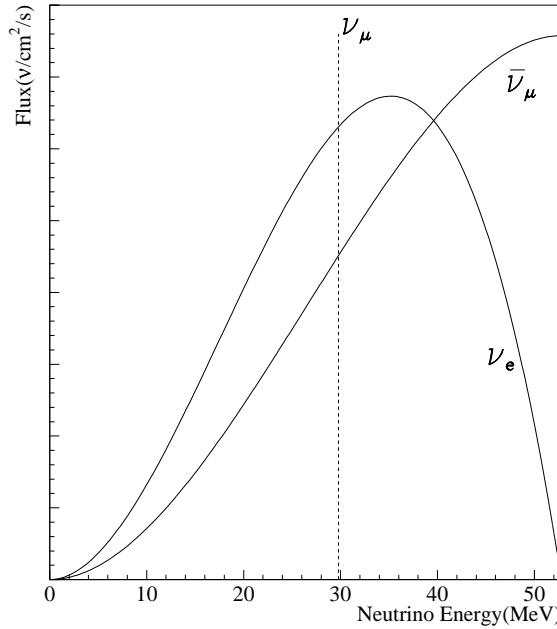


Figure 1: Flux shape of neutrinos from pion and muon decay at rest.

absorbed before they can decay. These stopped μ^- arise from π^- which decay in flight.

A few percent of the π^+ (π^-) produced at the beam dump decay in flight to ν_μ ($\bar{\nu}_\mu$) with energies up to 300 MeV. Those ν_μ above muon production threshold provide the source used for our measurement of $^{12}C(\nu_\mu, \mu^-)^{12}N^*$ [13]. In the analysis of the reaction $^{12}C(\nu_e, e^-)^{12}N^*$ presented in section 7 below we correct for a small background arising from μ^\pm produced by high energy ν_μ and $\bar{\nu}_\mu$.

The LANSCE beam dump has been used as the neutrino source for previous experiments[15, 16, 17]. A calibration experiment[18] measured the rate of stopped μ^+ from a low-intensity proton beam incident on an instrumented beam stop. The rate of stopped μ^+ per incident proton was measured as a function of several variables and used to fine-tune a beam dump simulation program[19]. The simulation program can then be used to calculate the flux for any particular beam dump configuration. The calibration experiment determined the DAR flux to $\pm 7\%$ for the proton energies and beam stop configurations used at LANSCE. This uncertainty provides the largest source of systematic error for the cross sections presented here. The LANSCE proton beam typically had a current of 800 μ A at the beam stop during the 1994-1995 running period and 1000 μ A for 1996-1997. For 1994 and 1995 the energy was approximately 770

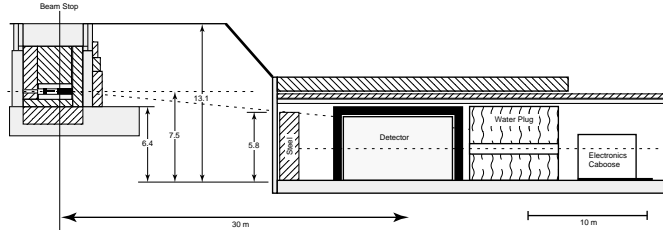


Figure 2: Detector enclosure and target area configuration, elevation view.

MeV at the beam stop due to energy loss in upstream targets, while it was approximately 800 MeV in 1996 and 1997. The water target was out for 32% of the 1995 data. Upstream targets contributed 1.4% to the DAR flux in 1994 and 1995. The DAR ν_e flux averaged over the LSND detector was $3.08 \times 10^{13} \text{ cm}^{-2}$ for 1994 and $3.45 \times 10^{13} \text{ cm}^{-2}$ for 1995.

The 1996-1998 data were obtained with the APT beam stop. There were no upstream targets for almost all of the data taking for this period. The DAR ν_e flux averaged over the LSND detector was $1.32 \times 10^{13} \text{ cm}^{-2}$ for 1996 and $2.73 \times 10^{13} \text{ cm}^{-2}$ for 1997. For the full data sample used in this paper the ν_e flux is $10.58 \times 10^{13} \text{ cm}^{-2}$.

3 The LSND Detector

The detector is located 29.8 m downstream of the proton beam stop at an angle of 12° to the proton beam. Figure 2 shows a side-view of the setup. Approximately 2000 g/cm^2 of shielding above the detector attenuates the hadronic component of cosmic rays to a negligible level. The detector is also well shielded from the beam stop so that beam associated neutrons are attenuated to a negligible level. Enclosing the detector, except on the bottom, is a highly efficient liquid scintillator veto shield which is essential to reduce contributions from the cosmic ray muon background to a low level. Reference [14] provides a detailed description of the detector, veto, and data acquisition system which we briefly review here.

The detector is an approximately cylindrical tank containing 167 metric tons of liquid scintillator and viewed by 1220 uniformly spaced 8" Hamamatsu photomultiplier tubes (PMT) covering 25% of the surface inside the tank wall. When the deposited energy in the tank exceeds a threshold of approximately 4 MeV electron-equivalent energy and there are fewer than 4 PMT hits in the veto shield, the digitized time and pulse height of each of these PMTs (and of each of the 292 veto shield PMTs) are recorded. A veto, imposed for $15.2 \mu\text{s}$ following the firing of > 5 veto PMTs, substantially reduces (10^{-3}) the large number of background events arising from the decay of cosmic ray muons that

stop in the detector. Activity in the detector or veto shield during the $51.2 \mu\text{s}$ preceding a primary trigger is also recorded, provided there are > 17 detector PMT hits or > 5 veto PMT hits. This activity information is used in the analysis to reject events arising from muon decay. Data after the primary event are recorded for 1 ms with a threshold of 21 PMTs (approximately 0.7 MeV electron-equivalent energy). This low threshold is used for the detection of 2.2 MeV γ from neutron capture on free protons. The processes measured in this paper, $^{12}\text{C}(\nu_e, e^-)^{12}N_{g.s.}$ and $^{12}\text{C}(\nu_e, e^-)^{12}N^*$, do not produce neutrons. Thus, in the present analysis, detection of 2.2 MeV γ s is used to help determine beam-related backgrounds with associated neutrons. The detector operates without reference to the beam spill, but the state of the beam is recorded with the event. Approximately 94% of the data is taken between beam spills. This allows an accurate measurement and subtraction of cosmic ray background surviving the event selection criteria.

Most triggers due to electrons from stopped muon decays (Michel electrons) are identified by a preceding activity produced by the decay muon. Occasionally, however the muon will not satisfy the activity threshold of > 17 detector PMT hits or > 5 veto PMT hits. For several LSND analyses, including the present one, it is desirable to further reduce the number of unidentified Michel electrons. Therefore, for data recorded after 1994 all PMT information was recorded for a period of $6 \mu\text{s}$ (2.7 muon lifetimes) preceding certain primary events. For the present analysis this “lookback” information is used to further reduce the cosmic ray muon background as described in Section 5.

The detector scintillator consists of mineral oil (CH_2) in which is dissolved a small concentration (0.031 g/l) of b-PBD[20]. This mixture allows the separation of Čerenkov light and scintillation light and produces about 33 photo-electrons per MeV of electron energy deposited in the oil. The combination of the two sources of light provides direction information for relativistic particles and makes particle identification (PID) possible. Note that the oil consists almost entirely of carbon and hydrogen. Isotopically the carbon is 1.1% ^{13}C and 98.9% ^{12}C .

The veto shield encloses the detector on all sides except the bottom. Additional counters were placed below the veto shield after the 1993 run to reduce cosmic ray background entering through the bottom support structure. More counters were added after the 1995 run. The main veto shield[21] consists of a 15-cm layer of liquid scintillator in an external tank and 15 cm of lead shot in an internal tank. This combination of active and passive shielding tags cosmic ray muons that stop in the lead shot. A veto inefficiency $< 10^{-5}$ is achieved with this detector for incident charged particles.

4 Analysis Techniques

Each event is reconstructed using the hit time and pulse height of all hit PMTs in the detector[14]. The present analysis relies on the reconstructed energy, position, direction, and two PID parameters, χ'_{tot} and α , as described later in this section. The particle direction is determined from the Čerenkov cone. The parameters χ'_{tot} and α are used to distinguish electron events from events arising from interactions of cosmic ray neutrons in the detector. We directly measure the response of the detector to electrons and neutrons in the energy range of interest for this analysis by using copious control data samples. We also use a GEANT Monte Carlo simulation, LSNDMC[22] to simulate events in the detector.

The response of the detector to electrons was determined from a large, essentially pure sample of electrons (and positrons) from the decay of stopped cosmic ray μ^\pm in the detector. The known energy spectra for electrons from muon decay was used to determine the absolute energy calibration, including its small variation over the volume of the detector. The energy resolution was determined from the shape of the electron energy spectrum and was found to be 6.6% at the 52.8 MeV end-point.

There are no tracking devices in the LSND detector. Thus, event positions must be determined solely from the PMT information. The reconstruction process determines an event position by minimizing a function χ_r which is based on the time of each PMT hit corrected for the travel time of light from the assumed event position to the PMT[14]. The procedure used in several previous analyses systematically shifted event positions away from the center of the detector and thus effectively reduced the fiducial volume[23]. The reconstruction procedure has been analyzed in detail and an improved reconstruction procedure was developed which reduces this systematic shift and provides substantially better position resolution. This procedure also provides results which agree well with positions obtained from the event likelihood procedure described in Ref. [24]. In the analysis presented in this paper, a fiducial cut is imposed by requiring $D > 35$ cm, where D is the distance between the reconstructed event position and the surface tangent to the faces of the PMTs. Events near the bottom of the detector ($y < -120$ cm) are also removed, as discussed in Section 5.

The particle identification procedure is designed to separate particles with velocities well above Čerenkov threshold from particles below Čerenkov threshold. The procedure makes use of the four parameters defined in Ref. [14]. Briefly, χ_r and χ_a are the quantities minimized for the determination of the event position and direction, χ_t is the fraction of PMT hits that occur more than 12 ns after the fitted event time and χ_{tot} is proportional to the product of χ_r , χ_a and χ_t .

Several previous LSND analyses [3, 13, 24] have used χ_{tot} for particle identification. The distribution of χ_{tot} for electrons, however, has a small variation with electron energy and with the position of the event. Therefore, in this pa-

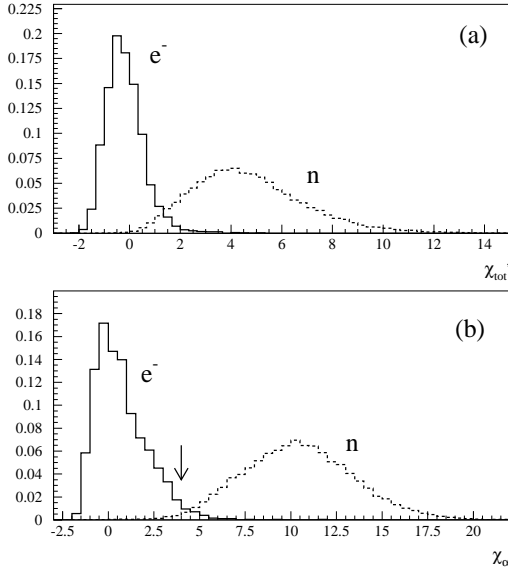


Figure 3: Particle identification parameters (a) χ'_{tot} and (b) χ_α for electrons and neutrons. In the present analysis we require $\chi_\alpha < 4.0$ as indicated by the arrow in (b).

per, we used a modified variable, χ'_{tot} , with a mean of zero and sigma of one, independent of the electron energy and positions. We also used the variable, α , which is based on the event likelihood procedures discussed in Ref. [24]. As in [24], α comes from a separate event reconstruction than that which produced χ'_{tot} . It is similar to the parameter ρ discussed there, which is based on the ratio of Čerenkov to scintillator light. The α parameter varies from 0 to 1 and peaks at one for electrons and at 0.3 for neutrons. The combination $\chi_\alpha = \chi'_{tot} + 10(1 - \alpha)$ provides better separation of electrons and neutrons than χ'_{tot} by itself.

Figure 3(a) shows the χ'_{tot} distribution for electrons from stopping μ decay and for cosmic ray neutrons with electron equivalent energies in the $18 < E_e < 50$ MeV range. Neutrons, after thermalizing, undergo a capture reaction, $n + p \rightarrow d + \gamma$. The 2.2 MeV γ 's are used to select a clean sample of neutron events. For a neutron E_e is the equivalent electron energy corresponding to the observed total charge. Figure 3(b) shows the χ_α distribution for the same events. In the present analysis we eliminate most cosmic ray neutron background by requiring $\chi_\alpha < 4.0$. We note that a modest particle identification requirement was imposed in the initial data processing that created the samples analyzed here. The effect of this requirement is also included in the analysis.

Beam-off data taken between beam spills play a crucial role in the analysis of this experiment. Most event selection criteria are designed to reduce the cosmic ray background while retaining high acceptance for the neutrino process of interest. Cosmic ray background which remains after all selection criteria have been applied is well measured with the beam-off data and subtracted using the duty ratio, the ratio of beam-on time to beam-off time. The subtraction was performed separately for each year's data using the measured duty ratio for that year. The ratio averaged over the full data sample was 0.0632. Beam-on and beam-off data have been compared to determine if there are any differences other than those arising from neutrino interactions. Any differences are small and the 1.1% uncertainty in the duty ratio introduces a negligible effect in the present analysis.

5 Electron Selection Criteria

In this section we describe the selection criteria used to obtain a clean sample of inclusive electrons arising from neutrino interactions in the detector. In the next section we present the analysis of the relatively pure sample of events from the process $^{12}C(\nu_e, e^-)^{12}N_{g.s.}$ which we obtain by requiring the detection of the positron from the β -decay of the $^{12}N_{g.s.}$. Section 7 then presents the analysis of the reaction $^{12}C(\nu_e, e^-)^{12}N^*$ using the sample of inclusive events without an identified positron from the β -decay of $^{12}N_{g.s.}$.

A lower limit of 18.0 MeV is imposed on the electron energy to eliminate the large cosmic ray background from ^{12}B β -decay as well as most 15.1 MeV gamma rays from the neutral current excitation of carbon. The ^{12}B nuclei arise from the absorption of stopped μ^- on ^{12}C nuclei in the detector. The scattered electron from the reaction $^{12}C(\nu_e, e^-)^{12}N_{g.s.}$ has a maximum kinetic energy of 35.5 MeV due to the Q value of 17.3 MeV. Allowing for energy resolution we impose an upper limit of 40 MeV on the electron energy.

The selection criteria and corresponding efficiencies for electrons with $18 \text{ MeV} < E_e < 40 \text{ MeV}$ are shown in Table 1. The reconstructed electron position is required to be a distance $D > 35 \text{ cm}$ from the surface tangent to the faces of the PMTs. The requirement $y > -120 \text{ cm}$ removes a small region at the bottom of the detector for which the cosmic ray background is relatively high due to the absence of a veto below the detector. There are 3.34×10^{30} ^{12}C nuclei within this fiducial volume. The fiducial volume efficiency, defined to be the ratio of the number of events reconstructed within the fiducial volume to the actual number within this volume, was determined to be 0.880 ± 0.055 . This efficiency is less than one because there is a systematic shift of reconstructed event positions away from the center of the detector as discussed in Section 4.

Several selection criteria are designed to further reject cosmic ray induced events. Events with more than three veto PMT hits or any bottom counter coincidence during the 500 ns event window are eliminated. The past activity

Table 1: The electron selection criteria and corresponding efficiencies for events with $18 \text{ MeV} < E_e < 40 \text{ MeV}$.

Quantity	Criteria	Efficiency
Fiducial volume	$D > 35 \text{ cm}$, $y > -120 \text{ cm}$	0.880 ± 0.055
Particle ID	$\chi_\alpha < 4$	0.940 ± 0.018
In-time veto	$< 4 \text{ PMTs}$	0.988 ± 0.010
Past activity	See text	0.635 ± 0.012
Future activity	$\Delta t_f > 8.8 \mu\text{s}$	0.991 ± 0.003
Lookback	likelihood	0.994 ± 0.004
DAQ and tape dead time	–	0.962 ± 0.010
Total		0.492 ± 0.035

cut is designed to reject most electron events arising from cosmic ray muons which stop in the detector and decay. This background has a time dependence given by the $2.2 \mu\text{s}$ muon lifetime. The past activity selection criteria reject all events with activity within the past $20 \mu\text{s}$ with > 5 veto PMT hits or > 17 detector PMT hits. We also reject any event with a past activity within $51 \mu\text{s}$ with > 5 veto PMT hits and > 500 detector PMT hits. A small (0.5%) loss of efficiency arises from a cut (made during initial data processing) on past activities that are spatially correlated with the primary event, within $30 \mu\text{s}$ of the primary event and have ≥ 4 veto PMT hits.

Muons which are misidentified as electrons are removed by requiring that there be no future activity consistent with a Michel electron. Any event with a future activity with fewer than 4 veto PMT hits and more than 50 detector PMT hits within $8.8 \mu\text{s}$ is rejected.

Cosmic ray muons which fire < 6 veto PMTs (10^{-3} probability) and stop in the iron walls of the detector will not register as past activities. Some of the decay electrons will radiate photons which will enter the detector and be reconstructed as electrons within the fiducial volume. In previous analyses we simply relied on the beam-off subtraction procedure to remove this background. Here we use the “lookback” information described in Section 3 to reject events from this source. This results in slightly smaller statistical errors in the final beam excess sample.

For primary events with > 300 PMT hits and no activity within the past $35 \mu\text{s}$ ($20 \mu\text{s}$) for 1995 data (1996-1998 data), we recorded all PMT information for the $6 \mu\text{s}$ interval proceeding the event. Muons with < 6 veto PMT hits will appear in this “lookback” interval as a cluster of veto PMT hits spatially correlated with the primary event. The distribution of time between the veto signals and the primary event should be consistent with the muon lifetime, and the distributions of veto PMT hits and veto pulse height should be consistent with that measured for muons producing < 6 veto PMT hits. We developed

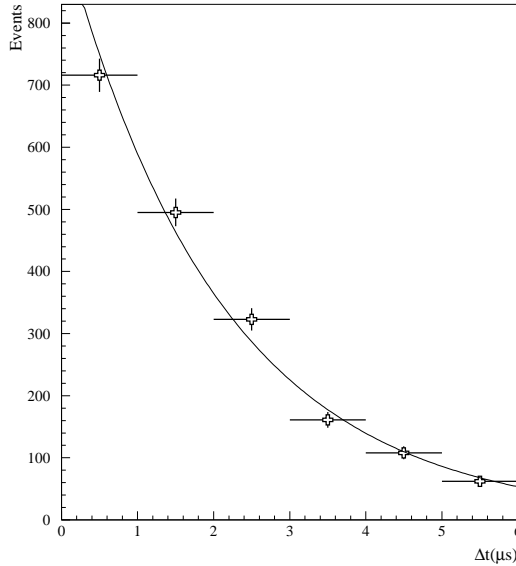


Figure 4: The distribution of time between the primary and the veto signal for beam-off events rejected using the “lookback” information compared with a curve corresponding to the muon lifetime.

a likelihood procedure based on these distributions which allowed us to reduce the beam off background by 9% with only a 0.6% loss of efficiency for neutrino events[25]. Figure 4 shows the time between the veto signal and the primary for rejected events.

The acceptances for the past activity, the future activity, the “lookback” and the in-time veto cuts are obtained by applying these cuts to a large sample of random events triggered with the laser used for detector calibration. These laser events are spread uniformly through the run and thus average over the small variation in run conditions. The acceptance for the $15.1 \mu s$ trigger veto is included in the past activity efficiency.

A sample of Michel electrons was analyzed to obtain the acceptance of electrons for the PID cut. Figure 5 compares the χ_α distribution of the inclusive electron sample with a Michel electron sample. The agreement is excellent. To eliminate any energy dependence, the Michel electrons are given weights as a function of energy so that the weighted spectrum agrees with the energy spectrum of electrons from the reaction $^{12}C(\nu_e, e^-)^{12}N_{g.s.}$. The acceptance, however, is very insensitive to the assumed energy spectrum. The beam excess distribution shown in Figure 5 is obtained by subtracting the beam off

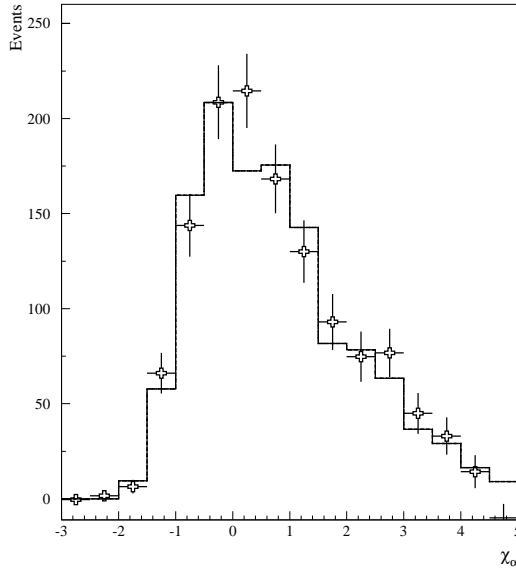


Figure 5: The χ_α distribution of the beam excess inclusive electron sample. The histogram shows the χ_α distribution of Michel electrons.

distribution from the beam on distribution as discussed in Section 3.

6 The Transition to the ^{12}N Ground State

The reaction $\nu_e + {}^{12}C \rightarrow e^- + {}^{12}N_{g.s.}$ is identified by the detection of the e^- , followed within 60 ms by the positron from the β -decay of the ${}^{12}N_{g.s.}$. Since we require at least $52\mu s$ β decay time, while transitions to excited states of ${}^{12}N$ decay by prompt photon emission, they do not feed down to the ${}^{12}N$ ground state or contribute to the delayed coincidence rate. The scattered electron has a maximum kinetic energy of 35.5 MeV due to the Q value of 17.33 MeV. The β -decay has a mean lifetime of 15.9 ms and maximum positron kinetic energy of 16.33 MeV. The cross section to the ${}^{12}N$ ground state has been calculated by several groups. The form factors required to calculate the cross section are well known from a variety of previous measurements. This cross section and the known ν_e flux are used to obtain the expected electron kinetic energy spectrum. Figure 6 shows the observed and expected electron energy distributions for events with an identified β -decay. Figure 7 shows the observed and expected spatial distributions of the same events. Both figures show good agreement with

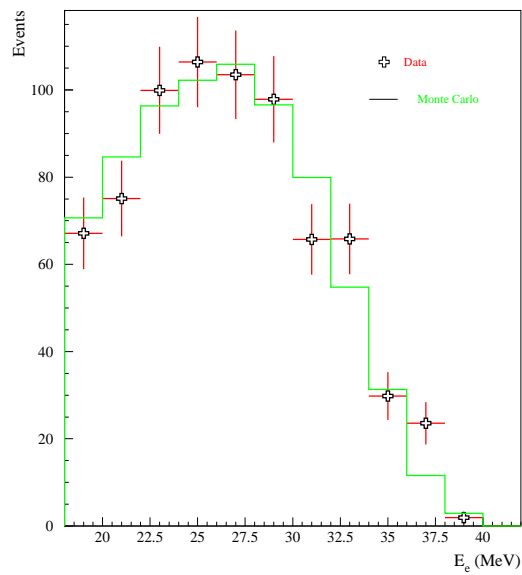


Figure 6: The observed and expected (solid line) energy distributions for electrons from $^{12}C(\nu_e, e^-)^{12}N_{g.s.}$.

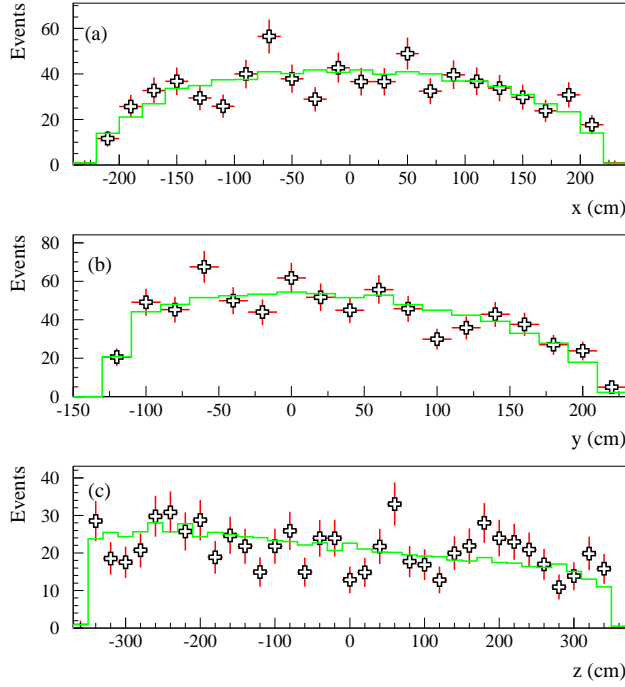


Figure 7: The spatial distribution of the electron for beam-excess events compared with expectation (solid line) from $^{12}C(\nu_e, e^-)^{12}N_{g.s.}$.

expectations.

Table 2 gives the selection criteria and efficiencies for the ^{12}N β -decay positron. Figure 8 shows the observed β -decay time distribution. The best fit curve yields a lifetime of 16.3 ± 0.8 ms in good agreement with the expected value of 15.9 ms. Figure 9 shows the distance between the reconstructed electron and positron positions for the beam-excess sample. A cut was applied at 0.7 m, resulting in an acceptance of $(99.2 \pm 0.8)\%$. Following an electron produced by a neutrino interaction, an uncorrelated particle, such as the positron from ^{12}B β -decay, will occasionally satisfy all the positron criteria including the requirements of time (60 ms) and spatial (0.7 m) correlation with the electron. The probability of such an accidental coincidence was measured by using the sample of Michel electrons. The inefficiency caused by the 15.1 μ s veto and the DAQ dead time are the same as for the electron. Positrons with 4 or more in-time veto hits or any bottom veto coincidence are rejected. The energy

Table 2: Criteria to select e^+ from $N_{g.s.}$ beta decay and corresponding efficiencies for the reaction $^{12}C(\nu_e, e^-)^{12}N_{g.s.}$.

Quantity	Criteria	Efficiency
β decay time	$52 \mu\text{s} < t < 60 \text{ ms}$	0.974 ± 0.002
Spatial correlation	$\Delta r < 0.7 \text{ m}$	0.992 ± 0.008
PMT threshold	> 100 for 1994, > 75 after 1994	0.856 ± 0.011
Fiducial volume	$D > 0 \text{ cm}$	0.986 ± 0.010
Trigger veto	$> 15.1 \mu\text{s}$	0.760 ± 0.010
In-time veto	$< 4 \text{ PMTs}$	0.988 ± 0.010
DAQ dead time		0.977 ± 0.010
Total		0.598 ± 0.015

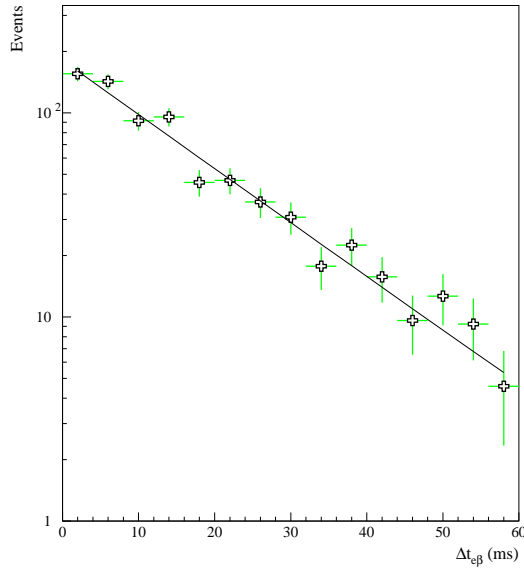


Figure 8: Distribution of time between the e^- and e^+ for beam excess events in the $^{12}C(\nu_e, e^-)^{12}N_{g.s.}$ sample. The best fit curve (solid line) corresponds to a lifetime of $16.3 \pm 0.8 \text{ ms}$.

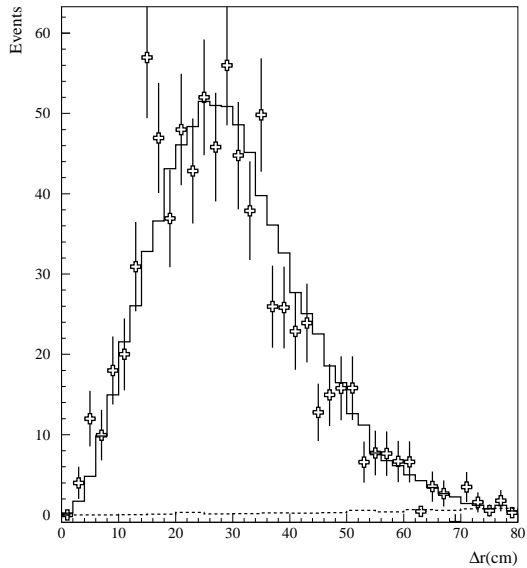


Figure 9: Distribution of the distance between the reconstructed positions of the e^- and e^+ for beam excess events in the $^{12}C(\nu_e, e^-)^{12}N_{g.s.}$ sample compared with Monte Carlo expectation (solid line). The calculated accidental contribution is shown by the dashed line.

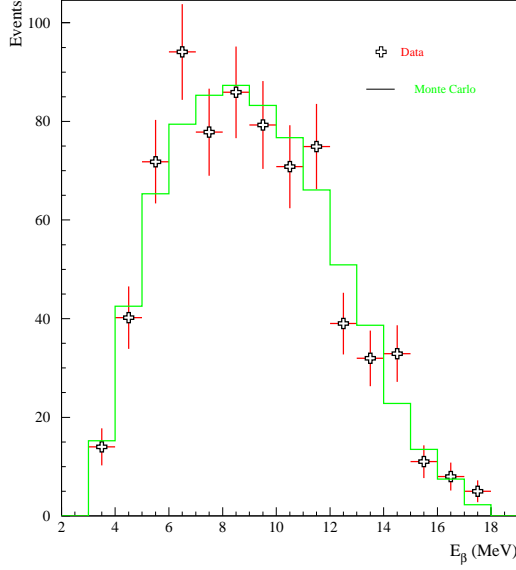


Figure 10: Observed and expected (solid line) e^+ energy distribution for the $^{12}C(\nu_e, e^-)^{12}N_{g.s.}$ sample.

distribution of the positron is calculated from the ^{12}N β -decay using

$$\frac{dN}{dE_e} = P_e E_e (E_{max} - E_e)^2 \times \frac{2\pi\eta}{(e^{2\pi\eta} - 1)} \quad (1)$$

where $\eta = Z\alpha/\beta_e$ and E_e is the total positron energy (including rest energy). The ^{12}N decays to the ground state ($E_{max} = 16.83$ MeV) 94.6% of the time. Beta decay transitions to the excited states of carbon are 1.9% ($E_{max} = 12.39$ MeV, followed by a 4.44 MeV γ), 2.7% ($E_{max} = 9.17$ MeV) and 0.8% ($E_{max} = 6.5$ MeV)[26]. The positron annihilates with an electron after stopping. The Monte Carlo was used to generate expected distributions for the positron energy and for number of hit PMTs. There was a trigger requirement of 100 PMT hits for 1994 data and 75 PMT hits after 1994. Figure 10 compares the observed and expected positron energy distributions. The good agreement shows that the energy calibration is valid for these low energy electrons.

Table 3 shows the electron and β selection efficiencies, the efficiency for satisfying the electron energy requirement and the total efficiency for the process $^{12}C(\nu_e, e^-)^{12}N_{g.s.}$. Table 4 provides a breakdown of the number of events satisfying the selection criteria as well as the total acceptance, the neutrino flux and the resulting flux averaged cross section. For the complete data sample the

Table 3: The electron and β selection efficiencies, the efficiency for satisfying the electron energy requirement and the total efficiency for the process $^{12}C(\nu_e, e^-)^{12}N_{g.s.}$

Quantity	Efficiency
Electron Selection	0.492 ± 0.035
Future β	0.598 ± 0.015
$18 \text{ MeV} < E_e < 40 \text{ MeV}$	0.789 ± 0.020
Total Efficiency	0.232 ± 0.019

Table 4: Events, efficiency, neutrino flux and flux averaged cross section with statistical error only for $^{12}C(\nu_e, e^-)^{12}N_{g.s.}$

Beam-on events	743
Beam-off events	6
Accidental background	4
Events from $^{12}C(\nu_e, e^-)^{12}N_{g.s.}$	733
Efficiency	0.232 ± 0.019
ν_e flux	$10.58 \times 10^{13} \text{ cm}^{-2}$
$\langle \sigma \rangle$	$(8.9 \pm 0.3) \times 10^{-42} \text{ cm}^2$

flux averaged cross section is $\langle \sigma \rangle = (8.9 \pm 0.3 \pm 0.9) \times 10^{-42} \text{ cm}^2$ where the first error is statistical and the second is systematic. The two dominant sources of systematic error are the neutrino flux (7%) discussed in Section 2 and the effective fiducial volume (6%) discussed in Section 4. The measured cross section decreases by 1.4% when the fiducial volume is reduced by requiring that the electron be at least 50 cm (instead 35 cm) from the surface of the PMT faces. As discussed in section 2 the beam stop was substantially modified after the 1995 run. The cross section measured for data taken with the modified beam dump is $(5 \pm 6(\text{stat.}))\%$ higher than for the initial beam dump and thus fully consistent within the statistical uncertainty. For comparison the previous measurements, the final LSND result and several theoretical predictions for the flux averaged cross section are presented in Table 5. They are all in agreement with each other.

For this reaction to the ^{12}N ground state it is also straightforward to measure the energy dependence of the cross section. The recoil energy of the ^{12}N nucleus is negligible and thus $E_\nu = E_e + 17.3 \text{ MeV}$ where E_e is the electron kinetic energy. Figure 11 shows that the energy dependence of the measured cross section agrees well with expectations[4]. Figure 12 shows the observed and expected[4, 28] angular distribution between the electron and the incident neutrino. The data agree well with expectations with the $\chi^2/DF = 0.79$. The mean observed value of $\cos \theta$ is $-0.046 \pm 0.021(\text{stat.}) \pm 0.030(\text{syst.})$ compared with an expected value of -0.068 . The systematic uncertainty in $\cos \theta$ is esti-

Table 5: Measurements and theoretical predictions of the flux averaged cross section for the process $^{12}\text{C}(\nu_e, e^-)^{12}\text{N}_{g.s.}$.

Experiment	
LSND	$(8.9 \pm 0.3 \pm 0.9) \times 10^{-42} \text{ cm}^2$
LSND(previous)[3]	$(9.1 \pm 0.4 \pm 0.9) \times 10^{-42} \text{ cm}^2$
E225[1]	$(10.5 \pm 1.0 \pm 1.0) \times 10^{-42} \text{ cm}^2$
KARMEN[2]	$(9.1 \pm 0.5 \pm 0.8) \times 10^{-42} \text{ cm}^2$

Theory	
Donnelly[5]	$9.4 \times 10^{-42} \text{ cm}^2$
Fukugita et al.[4]	$9.2 \times 10^{-42} \text{ cm}^2$
Kolbe et al.[7]	$8.9 \times 10^{-42} \text{ cm}^2$
Mintz et al.[27]	$8.0 \times 10^{-42} \text{ cm}^2$

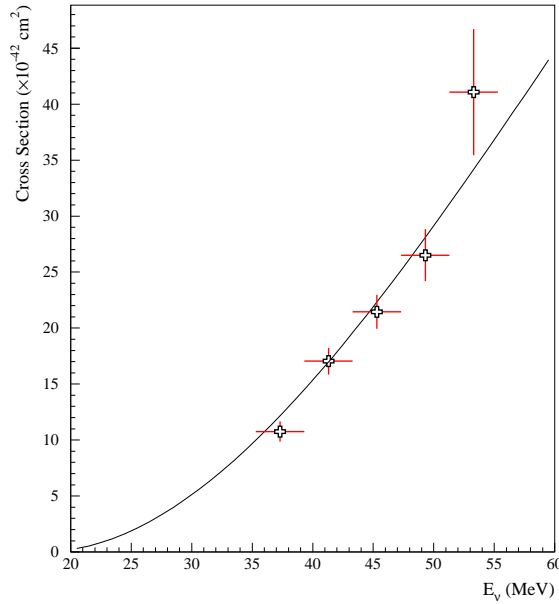


Figure 11: The measured and expected (solid line) cross section for the process $^{12}\text{C}(\nu_e, e^-)^{12}\text{N}_{g.s.}$.

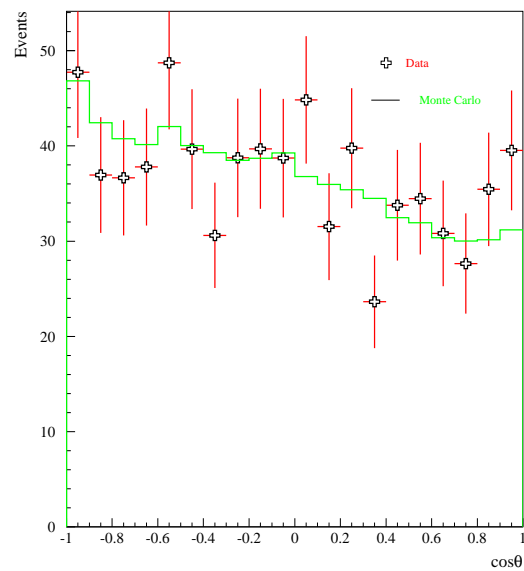


Figure 12: Observed and expected (solid line) distribution in $\cos\theta$ for the $^{12}C(\nu_e, e^-)^{12}N_{g.s.}$ sample, where θ is the angle between the e^- and the incident neutrino.

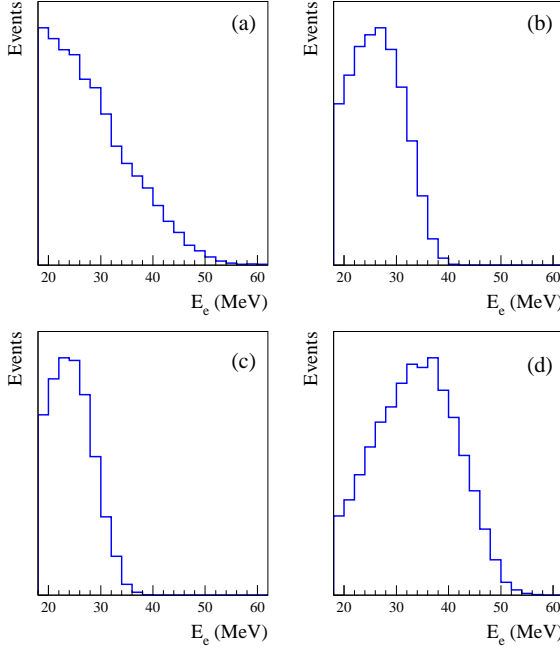


Figure 13: The expected distributions of electron energy for (a) νe^- elastic scattering, (b) $^{12}C(\nu_e, e^-)^{12}N_{g.s.}$, (c) $^{12}C(\nu_e, e^-)^{12}N^*$, and (d) $^{13}C(\nu_e, e^-)^{13}X$.

mated to be 0.030 based on Monte Carlo studies of the detector response. The expected $\cos\theta$ distribution shown in Figure 12 includes the effects of experimental resolution and as a result, is less backward peaked than the theoretical distribution used to generate it.

7 Transitions to excited states of ^{12}N

Electrons below 52 MeV are expected to arise from four major neutrino processes: $^{12}C(\nu_e, e^-)^{12}N_{g.s.}$, $^{12}C(\nu_e, e^-)^{12}N^*$, $^{13}C(\nu_e, e^-)^{13}X$ and neutrino elastic scattering. The expected energy and angular distributions of these processes are shown in Figures 13 and 14, respectively. The different event characteristics of these reactions are used to select a sample due primarily to the reaction $^{12}C(\nu_e, e^-)^{12}N^*$. This sample is then used to determine the flux averaged cross section and the electron energy and angular distributions for this reaction. The measured distributions are compared with expected distributions

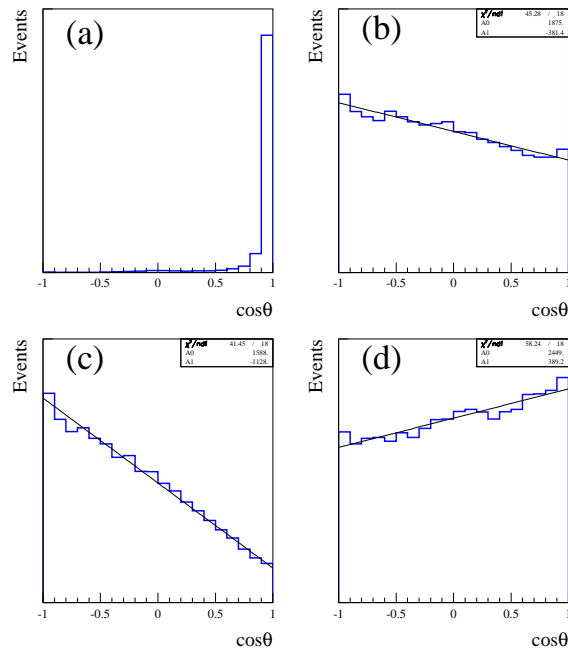


Figure 14: The expected distributions of $\cos\theta$ for (a) νe^- elastic scattering, (b) $^{12}C(\nu_e, e^-)^{12}N_{g.s.}$, (c) $^{12}C(\nu_e, e^-)^{12}N^*$, and (d) $^{13}C(\nu_e, e^-)^{13}X$. Straight line fits are shown in (b), (c) and (d).

Table 6: The electron selection efficiency, the efficiency for satisfying the β rejection criteria, the efficiencies for satisfying the angular and the energy requirements and the total efficiency for the process $^{12}C(\nu_e, e^-)^{12}N^*$

Quantity	Efficiency
Electron Selection	0.497 ± 0.035
No Future β	0.997 ± 0.001
$\cos \theta < 0.9$	0.980 ± 0.005
$18 \text{ MeV} < E_e < 34 \text{ MeV}$	0.687 ± 0.034
Total Efficiency	0.330 ± 0.029

for $^{12}C(\nu_e, e^-)^{12}N^*$ obtained from LSNDMC using the theoretical cross section of Ref. [28].

The reaction $^{12}C(\nu_e, e^-)^{12}N_{g.s.}$ is a source of background since the e^+ from the β -decay of $^{12}N_{g.s.}$ is not always identified. Any event with an identified e^+ in delayed coincidence is of course excluded. The background of events with an unidentified e^+ is calculated using the positron acceptance given in Table 2 and subtracted.

All three types of DAR neutrinos (ν_e, ν_μ and $\bar{\nu}_\mu$) elastically scatter off electrons in the detector but the rate is dominated by $\nu_e e^-$ scattering. The contribution due to DIF ν_μ and $\bar{\nu}_\mu$ scattering on electrons is almost negligible. The scattered electron for this process is strongly forward peaked as shown in Figure 14, and thus such events can largely be eliminated with the requirement $\cos \theta < 0.9$. A measurement of electron-neutrino electron elastic scattering by LSND is reported in a separate paper[29].

A third background arises from the interaction of ν_e on ^{13}C nuclei (1.1% of the carbon). The expected number of events obtained from the calculated cross section[5, 30] for this process is fairly small. The Q value is 2.1 MeV and thus about half of the background can be eliminated by requiring an electron energy below 34 MeV. We use the cross section calculated by Kubodera[30], $0.525 \times 10^{-40} \text{ cm}^2$, and conservatively assign a 50% uncertainty to this number. The KARMEN experiment has measured a cross section of $(0.5 \pm 0.37 \pm 0.1) \times 10^{-40} \text{ cm}^2$ for this reaction[31]. For this analysis the electron energy is required to be between 18 and 34 MeV. This region contains 68.7% of the excited state events simulated with LSNDMC using the cross section of Ref. [28]. The upper limit of 34 MeV not only eliminates much of the $^{13}C(\nu_e, e^-)^{13}X$ background, it further decreases the small background from the possible oscillation signal seen by LSND[23, 24].

Table 6 shows the efficiency for each selection criteria and the total efficiency for the process $^{12}C(\nu_e, e^-)^{12}N^*$. Table 7 shows the calculated number of background events from various sources satisfying these section criteria. In addition to the background sources already discussed, there are several smaller sources of background.

Table 7: Calculated number of background events satisfying the selection criteria for $^{12}C(\nu_e, e^-)^{12}N^*$. Systematic uncertainties in the numbers of background events are also shown.

Source	Events
$^{12}C(\nu_e, e^-)^{12}N_{g.s.}$	434.1 ± 28.1
$\nu e \rightarrow \nu e$	35.2 ± 4.1
$^{13}C(\nu_e, e^-)^{13}N$	46.6 ± 23.3
$^{12}C(\nu, \nu)^{12}C^*[15.1 \text{ MeV}]$	17.5 ± 2.0
$^{12}C(\nu_\mu, \mu^-)^{12}N^*$	9.3 ± 2.0
Events with a neutron	21.5 ± 15.1
Total Background	564 ± 40

The neutral current excitation $^{12}C(\nu, \nu)^{12}C^*$ ($1^+, 1$; 15.1 MeV) leads to prompt decay to photons with a 90% branching ratio. Most of the photons are eliminated by the 18 MeV energy requirement but approximately 0.8% will have reconstructed energies above 18 MeV due to the finite energy resolution. The measured cross section for this process[32, 33] is in good agreement with theoretical calculations[4, 5, 6].

As discussed earlier, LSND has also measured the process $^{12}C(\nu_\mu, \mu^-)^{12}N^*$ using a beam of ν_μ from π^+ DIF[13]. Normally we detect both the μ^- and the Michel e^- from the μ^- decay. Occasionally, however, we will miss a low energy μ^- because it does not satisfy the activity threshold of > 17 PMT hits. In that case the Michel electron will be a background event if it satisfies the selection criteria given in Table 6. We have calculated this background using the event simulation program LSNDMC. We have also estimated this background using the observed distribution of PMT hits for μ^- satisfying the activity threshold.

Finally, we determine the background from processes with associated neutrons. Events from the reactions $\bar{\nu}_e + p \rightarrow e^+ + n$ and $\bar{\nu}_\mu + p \rightarrow \mu^+ + n$ are identified in LSND by detecting the 2.2 MeV γ s from the capture reaction $n + p \rightarrow d + \gamma$ [3, 13, 23]. The mean capture time in the LSND detector is 186 μs , essentially independent of the initial neutron energy. Three variables are used to identify a capture γ correlated with a neutron in the primary event: the number of PMT hits for the γ , the distance of the γ from the primary event and the time of γ from the primary event. A likelihood technique, discussed in Ref. [23], has been developed to separate the correlated component due to neutrons from the uncorrelated or accidental component. An approximate likelihood ratio $R = \mathcal{L}_{\text{cor}}/\mathcal{L}_{\text{uncor}}$ is calculated for each event from the three measured variables. We use here an analysis with improved photon spatial reconstruction as is presented in Ref. [34], which reports final LSND results on neutrino oscillations.

Figure 15 shows the observed R distribution for events satisfying the selection criteria for the process $^{12}C(\nu_e, e^-)^{12}N^*$. Shown for comparison is the best

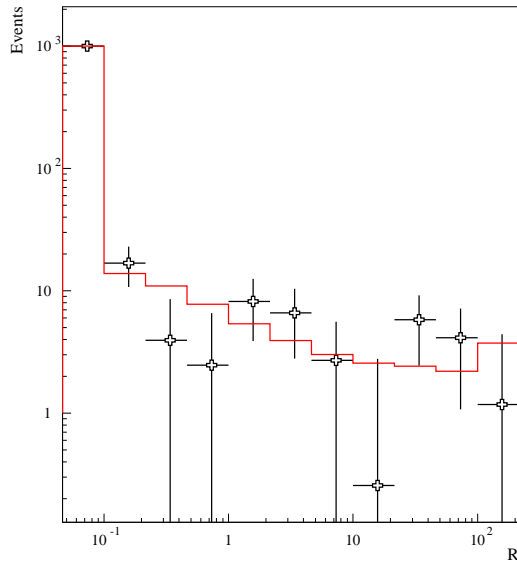


Figure 15: The observed distribution of the γ likelihood ratio R for the process $^{12}C(\nu_e, e^-)^{12}N^*$. Shown for comparison is the best fit (solid line) combination of the correlated distribution and the uncorrelated distribution to data. The best fit has a $2.0 \pm 1.4\%$ correlated component.

Table 8: Events, efficiency, neutrino flux and flux averaged cross section with statistical errors only for $^{12}C(\nu_e, e^-)^{12}N^*$

Beam-on events	2126
Beam-excess events	1088
Background	564
$^{12}C(\nu_e, e^-)^{12}N^*$	524
Efficiency	0.330 ± 0.029
Flux	$10.58 \times 10^{13} \text{ cm}^{-2}$
$\langle\sigma\rangle$	$(4.5 \pm 0.4) \times 10^{-42} \text{ cm}^2$

fit (solid line) combination of the correlated distribution and the uncorrelated distribution to the data. The best fit has a $2.0 \pm 1.4\%$ correlated component. The number of background events with neutrons shown in Table 7 is obtained from the best fit to the data.

Table 8 shows the number of beam-on and beam-excess events satisfying the selection criteria, the number of background events and the resulting number of events and cross section for the process $^{12}C(\nu_e, e^-)^{12}N^*$. It is worth noting that the beam-off subtraction is much larger in this case than it was for the exclusive reaction where we require a coincidence with a β . The flux average cross section is $\langle\sigma\rangle = (4.5 \pm 0.4 \pm 0.6) \times 10^{-42} \text{ cm}^2$. There are several contribution to the systematic error. The 7% flux uncertainty and the 6% uncertainty in the effective fiducial volume have been described previously[14]. There is a 4% uncertainty due to the 50% error in the ^{13}C cross section. The uncertainty in the e^+ acceptance for the $^{12}N_{g.s.}$ background subtraction leads to a 5% uncertainty in the $^{12}N^*$ cross section. The uncertainty in the duty ratio results in a 3% error in the cross section. We estimate a 5% uncertainty in the fraction of events with electrons in the region $18 \text{ MeV} < E_e < 34 \text{ MeV}$.

The cross section reported here is lower than that previously measured by LSND[3] primarily because of an increase in the calculated number of background events. (see Table 7). An increase in the calculated deadtime due to the veto lowered the β selection efficiency and increased the calculated number of events from the process $^{12}C(\nu_e, e^-)^{12}N_{g.s.}$ without an identified β . There was also an increase in the calculated number of events with $\cos\theta < 0.9$ from the process $\nu e \rightarrow \nu e$. The small DIF background from $^{12}C(\nu_\mu, \mu^-)^{12}N^*$ was not previously included. Finally, as was stated in Ref [3], we previously did not subtract the background from events with neutrons.

The flux averaged cross section measured by LSND is compared in Table 9 with other measurements and with several theoretical calculations. The most recent measurements of both LSND and KARMEN[31] are somewhat lower than their previous measurements[2, 3]. The recent CRPA result of Kolbe *et al.*[7], similarly, is lower than the previous result[6] but it remains above the cross section measurements of both LSND and KARMEN. In contrast the recent

Table 9: Measurements and theoretical predictions of the flux averaged cross section for the process $^{12}C(\nu_e, e^-)^{12}N^*$.

Experiment	
LSND	$(4.5 \pm 0.4 \pm 0.6) \times 10^{-42} \text{ cm}^2$
LSND(previous)[3]	$(5.7 \pm 0.6 \pm 0.6) \times 10^{-42} \text{ cm}^2$
E225[1, 35]	$(3.6 \pm 2.0) \times 10^{-42} \text{ cm}^2$
KARMEN[31]	$(5.1 \pm 0.6 \pm 0.5) \times 10^{-42} \text{ cm}^2$
Theory	
Kolbe et al.[6]	$6.3 \times 10^{-42} \text{ cm}^2$
Kolbe et al.[7]	$5.5 \times 10^{-42} \text{ cm}^2$
Hayes et al.[9]	$4.1 \times 10^{-42} \text{ cm}^2$

shell model calculation of Hayes and Towner[9] is in good agreement with but lower than the cross section measured by LSND.

Figure 16 shows that the measured electron energy distribution for the sample of events satisfying the electron criteria given in Table 6 agrees well with that expected from $^{12}C(\nu_e, e^-)^{12}N^*$ plus the background sources listed in Table 7. Also shown is the energy distribution expected from just the background processes. For the largest background source, $^{12}C(\nu_e, e^-)^{12}N_{g.s.}$, we used the shape of the energy distribution measured for a sample of events with identified β 's. For all other processes the expected energy distributions are obtained using simulated samples of events. Figure 17 compares the measured energy distribution after subtraction of the calculated backgrounds with the distribution expected for the process $^{12}C(\nu_e, e^-)^{12}N^*$. The agreement is excellent.

Figure 18 compares the measured distribution of $\cos\theta$ after subtraction of the calculated backgrounds with the distribution expected for the process $^{12}C(\nu_e, e^-)^{12}N^*$. The $\cos\theta$ distribution is enhanced in the backward direction as expected. The data are in fair agreement with expectations[28] with the $\chi^2/DF = 1.79$. The mean observed value of $\cos\theta$ is $-0.15 \pm 0.05(\text{stat.}) \pm 0.030(\text{syst.})$ compared with the expected value of -0.25 for Ref. [28] and -0.30 for Ref. [30]. The backward peaking of the angular distribution is largely a result of the negative parity of the N^* states expected to contribute, 2^- levels at 1.20 and 4.14 MeV and 1^- levels at 6.40 and 7.68 MeV. The $l = 1$ angular momentum transfer to the $A = 12$ system favors momentum transfer of approximately 100 MeV/c, and hence the backward peaking.

The total charged current cross section for ν_e interactions on ^{12}C is obtained by adding the cross sections measured for $^{12}C(\nu_e, e^-)^{12}N_{g.s.}$ and $^{12}C(\nu_e, e^-)^{12}N^*$. The resulting flux averaged cross section for $^{12}C(\nu_e, e^-)^{12}N$ is $\langle\sigma\rangle = (13.2 \pm 0.5 \pm 1.3) \times 10^{-42} \text{ cm}^2$.

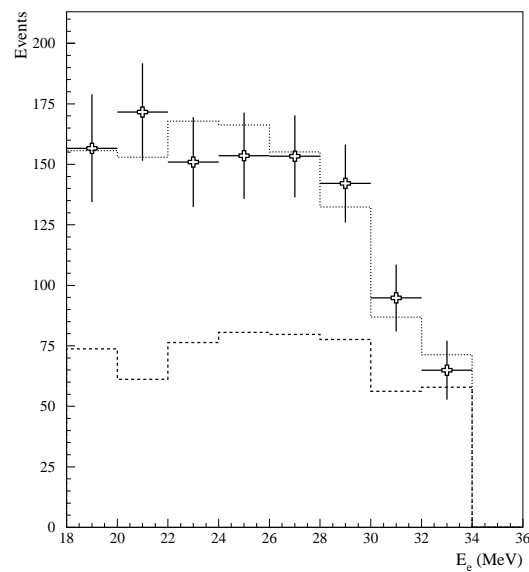


Figure 16: The observed distribution of electron energy for events satisfying the selection criteria given in Table 6. The dotted (dashed) histogram shows the expected distribution from all sources (background sources only).

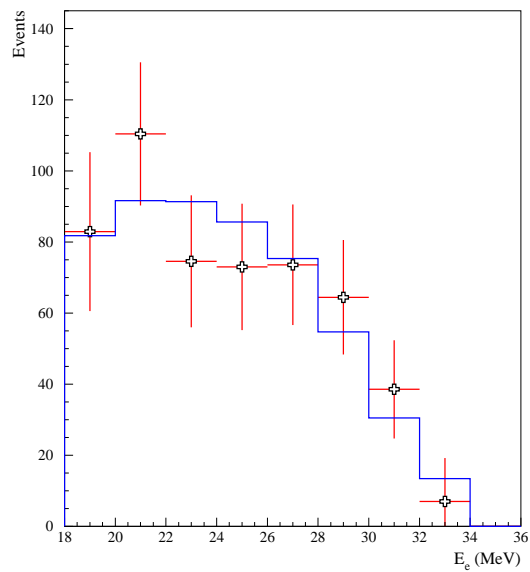


Figure 17: The observed and expected (solid line) electron energy distribution for the process $^{12}C(\nu_e, e^-)^{12}N^*$

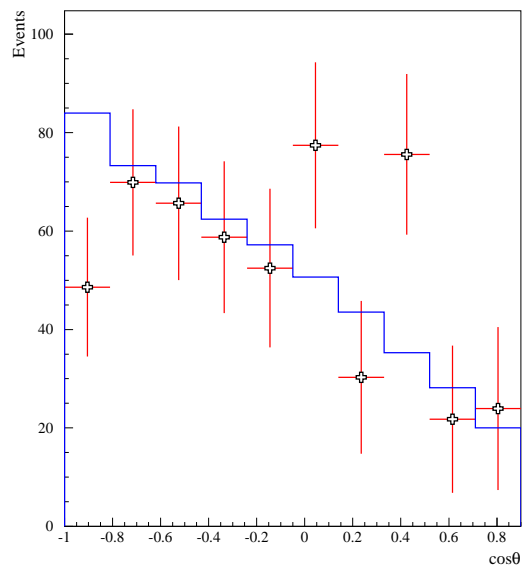


Figure 18: The observed and expected (solid line) $\cos \theta$ distribution for the process $^{12}C(\nu_e, e^-)^{12}N^*$

8 Conclusions

The process $^{12}C(\nu_e, e^-)^{12}N_{g.s.}$ has been measured with a clean sample of 733 events. For this process the cross section calculations using empirical form factors are expected to be very reliable. The flux averaged cross section is measured to be $(8.9 \pm 0.3 \pm 0.9) \times 10^{-42} \text{ cm}^2$ in reasonable agreement with other experiments and theoretical expectations. The energy and angular distributions also agree well with theoretical expectation.

The measurement of the process $^{12}C(\nu_e, e^-)^{12}N^*$ is more difficult, primarily due to the significant background subtraction required. The measured cross section of $(4.5 \pm 0.4 \pm 0.6) \times 10^{-42} \text{ cm}^2$ is in agreement with other measurements. It is in better agreement with the shell model calculation of Hayes and Towner [9] than with the CRPA calculation of Kolbe *et. al.*[7].

Acknowledgments This work was conducted under the auspices of the US Department of Energy, supported in part by funds provided by the University of California for the conduct of discretionary research by Los Alamos National Laboratory. This work was also supported by the National Science Foundation. We are particularly grateful for the extra effort that was made by these organizations to provide funds for running the accelerator at the end of the data taking period in 1995. It is pleasing that a number of undergraduate students from participating institutions were able to contribute significantly to the experiment.

References

- [1] D.A. Krakauer *et al.*, Phys. Rev. C **45**, 2450 (1992).
- [2] J. Kleinfeller *et al.*, in *Neutrino '96*, edited by K. Enquist, H. Huitu, and J. Maalampi (World Scientific, Singapore, 1997); B.E. Bodmann *et al.*, Phys. Lett. B **332**, 251 (1994); B. Zeitnitz, Prog. Part. Nucl. Phys. **32**, 351 (1994).
- [3] C. Athanassopoulos *et al.*, LSND Collaboration, Phys. Rev. C **55**, 2078 (1997).
- [4] M. Fukugia *et al.*, Phys. Lett. B **212**, 139 (1988).
- [5] T.W. Donnelly and R.D. Peccei, Phys Rep. **50**, 1 (1979); T.W. Donnelly, Phys. Lett. B **43**, 93 (1973).
- [6] E. Kolbe, K. Langanke, and S. Krewald, Phys. Rev. C **49**, 1122 (1994).
- [7] E. Kolbe, K. Langanke, and P. Vogel, Nucl. Phys. A **652**, 91 (1999).
- [8] C. Volpe *et al.*, Phys. Rev. C **62**, 015501 (2000).
- [9] A.C. Hayes and I.S. Towner, Phys. Rev. C **61**, 044603 (2000).
- [10] N. Auerbach, N. Van Giai, and O.K. Vorov, Phys. Rev. C **56**, R2368 (1997).
- [11] S.K. Singh, N.C. Mukhopadhyay, and E. Oset, Phys. Rev. C **57**, 2687 (1998).
- [12] T. Suzuki, D.F. Measday and J.P. Roalsvig, Phys. Rev. C **35**, 2212 (1987).
- [13] C. Athanassopoulos *et al.*, LSND Collaboration, Phys. Rev. C **56**, 2806 (1997).
- [14] C. Athanassopoulos *et al.*, LSND Collaboration, Nucl. Instrum. Methods Phys. Res. A **388**, 149 (1997).
- [15] S. Willis *et al.*, Phys. Rev. Lett. **44**, 522 (1980).
- [16] D.A. Krakauer *et al.*, Phys. Rev. C **45**, 2450 (1992).
- [17] S.J. Freedman *et al.*, Phys. Rev. D **47**, 811 (1993).
- [18] R.C. Allen *et al.*, Nucl. Instrum. Methods Phys. Res. A **284**, 347 (1989).
- [19] R.L. Burman, M.E. Potter, and E.S. Smith, Nucl. Instrum. Methods Phys. Res. A **291**, 621 (1990).
- [20] R.A. Reeder *et al.*, Nucl. Instrum. Methods Phys. Res. A **334**, 353 (1993).

- [21] J. Napolitano *et al.*, Nucl. Instrum. Methods Phys. Res. A **274**, 152 (1989).
- [22] K. McIlhany *et al.*, *Proceedings of the Conference on Computing in High Energy Physics*, 1994 (LBL Report 35822, 357, 1995).
- [23] C. Athanassopoulos *et al.*, LSND Collaboration, Phys. Rev. C **54**, 2685 (1996); C. Athanassopoulos *et al.*, LSND Collaboration, Phys. Rev. Lett. **77**, 3082 (1996).
- [24] C. Athanassopoulos *et al.*, Phys. Rev. C **58**, 2489 (1998), C. Athanassopoulos *et al.*, Phys. Rev. Lett. **81**, 1774 (1998).
- [25] N. Wadia, Ph.D. thesis, Louisiana State University, 1998.
- [26] F. Ajzenberg-Selove, Nucl. Phys. A **506**, 1 (1990).
- [27] S.L. Mintz and M. Pourkaviani, Phys. Rev. C **40**, 2458 (1989).
- [28] E. Kolbe, Phys. Rev. C **54**, 1741 (1996).
- [29] L.B. Auerbach *et al.*, LSND Collaboration, submitted to Phys. Rev. D.
- [30] M. Fukugita *et al.*, Phys. Rev. C **41**, 1359 (1990).
- [31] R. Maschuw, Prog. Part. Nucl. Phys. **40**, 183 (1998).
- [32] B. Bodmann *et al.*, Phys. Lett. B **267**, 321 (1991).
- [33] B. Armbruster *et al.*, Phys. Lett. B **423**, 15 (1998).
- [34] A. Aguilar *et al.*, LSND Collaboration, submitted to Phys. Rev. D. (Also submitted in hep-ex/0104040)
- [35] The quoted value of 3.6×10^{-42} cm², resulting from the subtraction of the ground state cross section from the inclusive cross section, is the preferred number of two values given in ref [1].